Integrated solar-driven high-temperature electrolysis operating with concentrated irradiation

Meng Lin[1,2,+], Clemens Suter[1,+], Stefan Diethelm[3], Jan van Herle[3], Sophia Haussener[1,4,*]

[1]Laboratory of Renewable Energy Science and Engineering, EPFL, 1015 Lausanne, Switzerland

[2]Department of Mechanical and Energy Engineering, Southern University of Science and Technology, Shenzhen 518055, China

[3]Group of Energy Materials, EPFL, 1951 Sion, Switzerland

[+] Equally contributing authors

[4]Lead contact

[*] Corresponding author: sophia.haussener@epfl.ch

Abstract

High-temperature electrolysis for reducing H_2O (and CO_2) to H_2 (and CO) converts concentrated solar energy into fuels and chemical feedstock. We invented an integrated reactor concept comprising a solar cavity-receiver for reactant heating, a solid oxide electrolyzer (SOE) stack for water electrolysis, and concentrated photovoltaic (PV) cells for the SOE stack's electricity demand. A numerical model compared thermoneutral and endo/exothermal operation of the SOE stack. Without heat recovery, we predicted a maximum solar-to-hydrogen (STH) efficiency of 19.85% (assuming 20% PV efficiency and 20% heat losses in the solar cavity-receiver) and preferentially endothermal operation. Heat recovery further improved the performance. We demonstrated a 2.5 kW (17% electrical, 83% thermal input) reactor, incorporating a commercial 16-cell Ni/YSZ/LSM SOE stack into a double-helical solar cavity-receiver, with 3.33% STH efficiency (assuming 20% PV efficiency). The experimentally-supported analysis indicates that endothermal operation increases the performance and predicts STH efficiencies encouraging intensified research and technology development.

1. Introduction

Co-electrolysis of H_2O and CO_2 to H_2 and CO (a mixture called synthesis gas and used as feedstock for Fischer Tropsch or methanol synthesis) driven by solar energy could be a promising route for the conversion of solar energy into storable fuels.[1–3] Solar-driven electrolysis of water at low temperatures (below 373 K), where the solar-electricity is provided by photovoltaic (PV) cells or concentrated solar power to drive a proton exchange membrane (PEM) electrolyzer,[4–8] are closest to commercial implementation and scaling (at least for hydrogen production). These systems have the potential to achieve a solar-to-hydrogen (STH) efficiency of more than 10%[9] (Si-based PV cells with solar-to-electricity (STE) efficiency of 20% and PEM electrolyzers with electricity-to-hydrogen (ETH) efficiency of 65%). However, PEM electrolysis requires rare and expensive noble metal catalysts (such as Pt, Ir or Ru), needs large overpotentials (~0.6 V for current densities in the range of 0.8 – 1 A cm^{-2}), and is not yet suitable for the selective reduction of CO_2 for co-electrolysis. High-temperature electrolysis using a solid oxide electrolysis (SOE) stack (typically operated at temperatures between 900 and 1200 K) overcomes these limits. The high operating temperatures result in faster reaction kinetics, enabling the use of earth-abundant catalysts (such as Ni).[10,11] From a thermodynamic point of view, the equilibrium potential is reduced at increased operating temperatures, and thus the electricity demand can be reduced (depending on the operation mode of the SOE stack).

One of the first experimental demonstration of a solar driven high-temperature electrolysis system was based on a tubular Pt/YSZ/Pt SOE stack placed in a ceramic tube surrounded by a glass dome. The ceramic tube served as solar absorber enabling indirect heating of the SOE stack, which was operated at 1273 K. The production of hydrogen was successfully demonstrated with an ETH efficiency (external electricity) of 71%. They predicted an overall STH efficiency in the range of 20 – 28%, assuming that the solar electricity was provided by thermoelectric elements using the heat from the outlet gases at 1073 K.[12] However, no details on the demonstrated thermal performance, in particular the solar-to-thermal (STT) efficiency of the solar absorber, have been revealed. Generally, the predictions of achievable STH efficiencies or the potential of solar-driven electrolysis depends strongly on the integration approach of electricity and heat and how these two carriers are produced.

Three main strategies for providing solar heat and electricity have been discussed: *i*) concentrated solar energy for heat and electricity from a thermal power cycle,[14–17] *ii*) PV cells for electricity and heat produced by resistive heaters,[18] and *iii*) the combination of both, i.e. concentrated solar energy for heat and PV cells or thermoelectric modules for electricity.[12,19] A techno-economic analysis has shown that strategy *iii*) with PV for electricity predicts the best trade-off between high STT efficiency and moderate costs for PV electricity, resulting in a solar-to-fuel (STF) efficiency of ~10%.[18] Systems using concentrated solar energy for heat and PV cells or thermoelectric modules for electricity typically consist of three distinctly separated (decoupled) components: *i*) a solar cavity-receiver (heat), *ii*) PV cells or thermoelectric modules (electricity),[12] and *iii*) a SOE stack (electrochemistry). These components are connected by tubes (fluidics) and wires (electrics).[15,18]

The optimum aperture size of the solar cavity-receiver for the production of high-temperature heat results from a compromise between maximizing radiation capture and minimizing reradiation losses.[20] The reduction of heat conduction losses through the jacket of the solar cavity-receiver requires the use of high-quality insulation. Furthermore, solar cavity-receivers for direct steam generation – as required for high-temperature electrolysis of water – involve complex heat and mass transfer characteristics, coupling conduction, convection and radiation in the solar cavity-receiver and two-phase flow phenomena in the tubes, inducing complicated heat transfer phenomena.[21–23] Heat recovery from the outlet gas streams is recommended in order to compensate for the heating penalty because of reactant heating (which is not needed for room-temperature electrolysis). However, heat recovery is expensive,[17–19] especially at high temperatures. PV cells for the electricity supply can either be placed close to the aperture of the solar cavity-receiver (requiring the use of triple junction, III-V material based cells) or separately placed from the concentrated irradiation (allowing for the use of commercial Si-based cells). Electric losses result from the coupling between the PV cells and the SOE stack, in particular from a mismatch between the maximum power point of the PV cells and the operating current and voltage of the SOE stack. Thus, control strategies such as mass flow rate adaptations,[24] or the use of a DC-DC converter are required. Generally, the thermoneutral (or near thermoneutral) operation of the SOE stack is meaningful as: *i*) neither heat is produced nor removed, and thus a stable temperature in the SOE stack is achieved, and *ii*) reasonable current densities and thus reasonable hydrogen production rates are achieved.[10] Thus, thermoneutral operation is recommended for standard (non-solar) SOE applications. Endothermal operation of the SOE stack allows for reduced electricity demand (given by the decreased equilibrium potential), which is compensated by additional heat, and results in higher ETH efficiencies but reduced current density (compared to thermoneutral operation). Endothermal operation might be advantageous in the context of solar energy integration to SOE, considering that both, heat and electricity, can be provided by solar energy to the SOE stack and that heat is produced more efficiently than electricity from solar energy.

An example of an experimental demonstration of solar high-temperature electrolysis via a separate solar cavity-receiver to produce steam that was transmitted to a separate SOE stack operated in the dark has been reported.[25] They operated the SOEC stack at 1050 K and with a current density of 12'500 A m^{-2} (slightly exothermal), reporting 70% steam conversion and 93% ETH efficiency. No details on the performance, such as STH efficiency, have been revealed. However, transmission losses – heat and pressure losses occurring in the tubes connecting the solar cavity-receiver to the SOE stack – are expected in such a decoupled operational mode. These losses have been estimated to result in a temperature drop of around 300 K or a reduction in the STF efficiency of approximately 30% (STF efficiency drop from 18.6% to 12.3% has been predicted).[26] Thus, we propose an integrated design approach to overcome these transmission losses where the solar cavity-receiver and the SOE stack build a single unit (termed integrated solar reactor).

The experimental implementation of an integrated design is challenging given the thermo-mechanical stress of the SOE stack (brittle ceramics), which is exposed to non-uniform and intermittent concentrated solar radiation. Additionally, a small temperature difference (below 100

K) is required at the outlets of the anodic and cathodic streams in order to keep the temperature gradients in the SOE stack below 10 K cm^{-1}.[13] These challenges require advanced component design (e.g. tubular SOE cell serving at the same time as solar absorber for transmission loss reduction) and thermal management (e.g. large enough reactant flow rates in order to deal with thermo-mechanical stress in the SOE stack). Up to now, these challenges have prevented the successful experimental demonstration of the integrated design. Even in such an integrated design, all the physical steps (heat absorption, electrochemical reactions, photoelecrical process) occur at different locations and at different times and, therefore, (microscopic) photothermal or photocatalytic effects (in semiconductors) are not present.

Here, we will demonstrate that the integration of a solar cavity-receiver and a high-temperature SOE stack into a single device provide a unique performance advantage. Back of the envelope calculations show that such an integrated system can be more performant than systems that are made of separate PV plus SOE components or a PV plus PEM electrolysis components (see Supplementary Note 1). We will utilize a coupled heat transfer model of the solar cavity-receiver with an electrochemical SOE stack model to provide guidance of optimal operation and design. Specifically, the comparison and advantages of endothermal operation over thermoneutral operation will be quantified. Subsequently, we demonstrate the integrated reactor concept with concentrated solar irradiation at 2.5 kW peak input power (17% electrical and 83% thermal).

2. Results
2.1 Model predictions
The STH efficiency depends mainly on the STT efficiency of the solar cavity-receiver, the electrochemical performance of the SOE stack, and the STE efficiency of the PV cells. The goal was to investigate the effect of the solar thermal input, the current density and the three operation modes of the SOE stack on the STH efficiency, in particular the endothermal operation, which enables the benefit of high-temperature electrolysis (decrease of Gibbs energy, and thus reduced electricity demand). The reference case was defined as *i*) 20% heat loss in the solar cavity-receiver ($f_{loss} = 0.2$, see definition in section 4.2), *ii*) solar concentration of 500 at the aperture ($\tilde{C} = 500$, A_{aper} variable), *iii*) no heat recovery ($\eta_{HR} = 0$ equivalent to $\eta_{HX} = 0$, see definitions in section 4.2), and *iv*) overstoichiometry of 2 ($f_{overstoch} = 2$, see definition in section 4.3).[27] All model parameters are listed in Table 1. Variant cases with respect to the reference case are *i*) heat recovery of 80% and *ii*) improved SOE stack performance with reduced overpotentials. For the latter case, we representatively removed the activation overpotentials(thus $V_{cell} = E + \eta_{ohmic} + \eta_{conc,a} + \eta_{conc,a}$ in eq. (2)), one of the two dominating overpotentials ($\eta_{ohmic}, \eta_{act,i}$).

Area-specific quantities are used in the following analyses, such as $q_{solar,th} = \dot{Q}_{solar,th} / A_{stack}$, $q_{solar,PV} = \dot{Q}_{solar,PV} / A_{stack}$ and $q_{stack} = \dot{Q}_{stack} / A_{stack}$ (see definitions of $\dot{Q}_{solar,th}$, $\dot{Q}_{solar,PV}$ and $\dot{Q}_{stack}$ in eq. (1), eq. (4), and eq (3), respectively, note the stack area is constant, the aperture area is variable). The temperature of the solar cavity-receiver and the stack as a function of the solar thermal input and current density for the reference case is shown in Figure 1a. The solar cavity-receiver temperature

4

(red isolines) is monotonically increasing with increasing solar thermal input whereas it is monotonically decreasing with increasing current density due to the variable mass flow rate (mass flow rate increases linearly with increasing current density due to $f_{overstoich} = 2$). The solar cavity-receiver temperature ranges from 500 K to 1500 K. The lowest STT efficiency was $\eta_{STT} = 18.3\%$ (see definition in eq. (5)) achieved at the highest temperature. The highest STT efficiency was $\eta_{STT} = 79.5\%$ achieved at the lowest temperature (see Figure S4 for STT efficiency as a function of solar thermal input and current density). The corresponding operation mode of the SOE stack (i.e. its heat flux) is shown in Figure 1b (red isolines). The stack temperature is higher than the cavity temperature for operation in the exothermal mode of the SOE stack (above thermoneutral isoline, i.e. $q_{stack} > 0$) whereas for the endothermal operation (below thermoneutral isoline, i.e. $q_{stack} < 0$) we observed the opposite. As an example for extreme exothermal operation of $q_{stack} > 1000$ W m^{-2} ($q_{solar,th} = 1420$ W m^{-2} and $j = 5000$ A m^{-2}), we observed a temperature difference between the cavity and the stack of more than 400 K ($T_{cav} \sim 500$ K and $T_{stack} \sim 900$ K). However, these conditions are not favorable given the large overpotential losses in the SOE stack coming from the low stack temperatures ($T_{stack} < 1000$ K) resulting in a non-optimum STH efficiency.

The highest STH efficiency (green asterisk, see definition in eq. (8)) was predicted to be 19.85%[†] for $q_{solar,th} = 910$ W m^{-2} and $q_{solar,PV} = 5213$ W m^{-2} ($j = 820$ A m^{-2}). The corresponding solar cavity-receiver and stack temperatures were 1117 K and 981 K, respectively. Note that the STT efficiency was 62.3%. The highest STH efficiency was achieved for endothermal conditions ($q_{stack} = -82.6$ W m^{-2}). The corresponding limiting STH efficiency ($\eta_{STH,limit}$, see definition in eq. (9)) would be 23.84%, which is only 3.99% higher than the maximum STH efficiency predicted by the lumped parameter model. The difference between the limiting STH efficiency and the simulated maximum STH efficiency is attributed to the additional solar thermal input penalty accounting for multiple species (sweep gas and H$_2$), the overstoichiometry in the reactant heating and the overpotential losses in the SOE stack. For $\eta_{STH} > 19\%$ in Figure 1b (yellow area in contour plot), we observe a large operation range (band), namely $q_{solar,th} = 1000 - 4000$ W m^{-2} and $j = 500 - 4000$ A m^{-2} with quasi linear relation between solar thermal input and current density. Thus, a good trade-off between high STH efficiency and high production rate of H$_2$ can be achieved by running at appropriate current densities and solar thermal inputs, for example, at $q_{solar,th} = 3000$ W m^{-2} and $j = 3000$ A m^{-2}. The band with $\eta_{STH} \sim 19\%$ also reveals that the SOE stack can be operated in all three modes (marginal differences in STH efficiency of ~0.5%). Thus, the thermoneutral operation might be recommended as it is the safest (in terms of thermo-mechanical stress to the SOE stack). We observed even for the thermoneutral isoline that $\eta_{STH} > \eta_{PV} \cdot \eta_{DC-DC} = 18.6\%$, which indicates that the STH efficiency is higher than the pure conversion of solar radiation to electricity available for the SOE stack (PV and DC-DC converter). Thus, the penalty of solar thermal input for reactant heating is fully compensated by the gain of reduced reaction enthalpy resulting from evaporation of water. Note that the reaction enthalpy per mole of produced hydrogen is 248 kJ mol^{-1} for

---

[†] For other solar concentrations ($\tilde{C} = 250$ and $\tilde{C} = 750$, see Figure S6), we observed that the maximum STH efficiency was marginally different (19.53% for $\tilde{C} = 250$ and 19.98% for $\tilde{C} = 750$, respectively).

maximum STH efficiency conditions (T_{stack} = 981 K). We observed that the electricity demand was 228 kJ mol^{-1}, and thus reduced by 20 kJ mol^{-1} (limiting reduction would be 54 kJ mol^{-1}), showing the effect of the endothermal operation. The rather large solar input factor (f_{solar}, see definition in eq. (6)) of ~15% indicates that the heat recovery is useful to further decrease the contribution of solar thermal input compared to the total solar input.

The Sankey diagram in Figure 2 shows for the highest STH efficiency case (indicated by the green asterisk in Figure 1b) the conversion of the solar thermal and electrical input to hydrogen, highlighting the energy losses. The solar electric input ($\dot{Q}_{\text{solar,PV}}$ = 225.2 W) is 5.7 times higher than the solar thermal input ($\dot{Q}_{\text{solar,th}}$ = 39.3 W) . The largest losses occur in the PV cells ($\dot{Q}_{\text{PV,loss}}$ = 180.2 W), corresponding to 68.1% of the total solar input. The endothermal operation of the SOE stack ($\dot{Q}_{\text{stack}}$ = 3.6 W) together with the heat for the evaporation ($\dot{Q}_{\text{evap}}$ = 7.0 W) of the reactant (liquid water), which is transformed to hydrogen, is used for reducing the reaction enthalpy, and thus the electricity demand. We observe that the heat of the stack and the heat of evaporation are the only flows from the thermal process into the electrical process. The produced hydrogen ($\Delta\dot{n}_{\text{H}_2} \cdot HHV_{\text{H}_2}$ = 52.5 W) is larger in power (by 10.6 W) than the used electricity demand (P_{stack} = 41.9 W). Note that heat for evaporation of excess water (given by overstoichiometry) cannot be used and leaves the thermal process together with the other gases (i.e. ΔH_{stack} = 13.9 W). Given ΔH_{stack} = 13.9 W, we conclude that the maximum heat recovery is η_{HR} = 35.4% $\cong \eta_{\text{HX}}$ = 100%, resulting from ΔH_{stack} / $\dot{Q}_{\text{solar,th}}$, thus we investigated η_{HR} = 30% $\cong \eta_{\text{HX}}$ = 83.8% (see Figure S7 for η_{HR} = 10% $\cong \eta_{\text{HX}}$ = 28.8% and η_{HR} = 20% $\cong \eta_{\text{HX}}$ = 59.3%).

We observed for the case with heat recovery effectiveness of 30% (other parameters kept at reference case values), analogously to the reference case, a large operation range at high efficiency (η_{STH} > 20.0%, yellow area) see Figure 1c. A maximum STH efficiency of 20.83% was predicted for $q_{\text{solar,th}}$ = 636 W m^{-2} and $q_{\text{solar,PV}}$ = 4630 W m^{-2} (T_{stack} = 1002 K and j = 740 A m^{-2}), and thus an increase of 0.98% compared to the reference case without heat recovery. The relatively small increase in STH efficiency is attributed to the observation that the dominating losses appear in the STE conversion (η_{PV} = 20%). The solar input factor was decreased from 15% (reference case without heat recovery) to 12% as expected from the heat recovery due to the reduced required solar thermal input. Similarly to the reference case without heat recovery, the maximum STH efficiency case lies in the endothermal operation range, i.e. q_{stack} = -88.9 W m^{-2}. The electricity demand is 225 kJ mol^{-1}, and thus a reduction of 23 kJ mol^{-1}. Considering η_{PV} = 20% and η_{STH} > 20% (yellow area in Figure 1c), we observe that the STH efficiency is higher than the STE efficiency. This emphasizes that the gain (reduced solar electrical input for the SOE stack given by the endothermal operation and reduced reaction enthalpy resulting from evaporated water) fully compensates the penalty of solar thermal input for reactant heating and internal electrical losses (DC DC conversion) – termed as thermal and electrical penalty – and, thus, the high-temperature electrolysis becomes beneficial. Note that η_{STH} is smaller than 20% for the thermoneutral operation (isoline at q_{stack} = 0) and the thermal and electrical penalty is never compensated (thermoneutral isoline lies outside the

yellow area). We found that $\eta_{HR} > 10\% \triangleq \eta_{HX} > 38.8\%$ is required for achieving $\eta_{STH} > 20\%$ (in a large operation band) and the high-temperature electrolysis becomes beneficial (see Figure S7). The analysis of the case with an improved SOE stack (reduced overpotentials, see Figure 1d) revealed a different behavior. The operation range with $\eta_{STH} > 20\%$ is shifted towards the lower temperature bound ($T_{stack} = 900$ K), and thus the potential of optimization is limited by the lower stack temperature constraint. The operation range shows a clear endothermal operation with q_{stack} ranging from -150 to -400 W m^{-2} (no other operation modes, in contrast to the reference case), thus the reduced overpotentials favor the endothermal operation. The maximum STH efficiency of 21.16% is found for $q_{solar,th} = 909$ W m^{-2} and $q_{solar,PV} = 3995$ W m^{-2} ($T_{stack} = 893$ K and $j = 700$ A m^{-2}), in endothermal mode ($q_{stack} = -153$ W m^{-2}). The electricity demand is 205 kJ mol^{-1} (compared to the reaction enthalpy of 247 kJ mol^{-1} for $T_{stack} = 893$ K), and thus the reduction is 42 kJ mol^{-1}, which is close to the thermodynamic limit of 48.4 kJ mol^{-1}. We observe that the high-temperature electrolysis is already beneficial without any heat recovery as $\eta_{STH} > 20\%$, (thermal and electrical penalty is always compensated).

2.2. Experimental demonstration

We aimed at operating the integrated solar reactor at $T_{stack} = 950 - 1050$ K and for thermoneutral operation mode based on the model predictions (reference case, no heat recovery), resulting in safer experimental operation conditions (less thermo-mechanical stress in the SOE stack). Endothermal operation was not possible given the large temperatures required and the corresponding safety concerns with the solar receiver.

Transient characteristics – The transient behavior of the solar cavity-receiver was tested for SFC-open circuit conditions for SFC 4/4 and 8/8 and for $\dot{Q}_{solar,th} = 1.0 - 2.1$ kW (campaign 1, type 2). The maximum $T_{cav} = 1104$ K was achieved for SFC 4/4 and $\dot{Q}_{solar,th} = 2.1$ kW. The experimentally determined thermal time constant ranged from $\tau = 5.94 - 14.2$ min for SFC 8/8 and $\tau = 2.9 - 8.9$ min for SFC 4/4. A lumped parameter thermal equivalent resistance network model (see Supplementary Note 5), considering radiative heat transfer in the solar cavity-receiver (external) and heat convection from the absorber tubes to the reactant flows (internal), predicted a decreasing thermal time constant with increasing solar thermal input as the radiative heat transfer increases with the temperature to the power of 4. The thermal equivalent resistance network model indicated that the SFC has no effect on the convective heat transfer (Nusselt number in laminar flows in fully developed flows in circular pipes is independent of mass flow rate), which was experimentally confirmed. Both the radiative and convective heat transfer modes were of the same order of magnitude, thus no heat transfer mode was dominant. This indicates that the overall heat transfer starting from solar radiation and ending in absorbed heat in the solar cavity-receiver has no bottleneck, and thus the current configuration (geometry of solar cavity-receiver, flow rates) is well matched to the solar thermal input.

Thermal efficiency – The thermal performance of the solar cavity-receiver was tested for thermal-only (campaign 1, type 1) and SFC-open circuit conditions (campaign 1, type 2) at steady state.

7

Figure 3a shows the experimentally measured STT efficiency as a function of the measured solar cavity-receiver temperature. The STT efficiency decreases monotonically with increasing temperature. The temperature increases as a result of a decrease in the mass flow rate (for both types) and an increase in the solar thermal input for type 2 data only (solar thermal input was constant for type 1 data). The highest measured STT efficiency of 76.5% was achieved for T_{cav} = 725 K for type 1 experiments, resulting from the highest flow rate of N_2 of 1 Nl min^{-1} and H_2O of 12.6 g min^{-1}. 21.3% of $\dot{Q}_{solar,th}$ was lost by heat losses ($\dot{Q}_{loss}$ = 194 W, see definition in eq. (1)), and 2.2% by reradiation ($\dot{Q}_{reradiation}$ = 20 W, see definition in eq. (1)). However, the rather low cavity temperature is not suited for SOE stack operation, requiring cavity temperatures at the upper limit (T_{cav} = 975 K). At these high temperatures, we observed the lowest STT efficiency, i.e. η_{STT} = 16% (for N_2 flow rate of 0.18 Nl min^{-1} and H_2O of 2.25 g min^{-1}). The heat losses were 77% of the solar thermal input and the reradation losses 7%, indicating that $\dot{Q}_{loss}$ is dominant compared to $\dot{Q}_{reradiation}$.

The STT efficiency of an ideal cavity-receiver (20% heat losses, $\tilde{C}$ = 724, eq. (7)) has a limit at $\eta_{STT,limit}$ = 78% for T_{cav} = 700 K and $\eta_{STT,limit}$ = 69% for T_{cav} = 1100 K. We observe agreement between the ideal (see definition in eq. (7)) and experimental STT efficiency results for low cavity temperatures whereas for high cavity temperatures, the experimental STT efficiency was drastically lower (53% lower), which is attributed to the heat losses, which increase non-linearly with increasing cavity temperature (21.3 – 77%).

We measured even lower STT efficiencies (ranging from 6.8 – 20.2%) for type 2 experiments. The heat losses were high throughout all solar thermal inputs and SFCs and ranged from 78 – 88%. The lower STT efficiencies are attributed to the installed SOE stack (which was not the case for type 1 experiments), and thus causing larger heat losses due to less dense insulation. Thus, we identify a large potential of the current solar cavity-receiver for improvement in STT efficiency by reducing the heat losses. Separation of the hot parts (double helix) from the cold parts (water-cooled steel front) and insulation of void spaces will reduce these heat losses.

Characteristics of SOE stack – The current (density) and voltage characteristics (referred to as *I-V* curves) of the SOE stack were characterized *in-situ* and are shown in Figure 3b. The current and the current density monotonically increase with increasing stack voltage (and cell voltage), for both SFCs and for all $\dot{Q}_{solar,th}$. The thermoneutral voltage was V_{stack} = 20.8 V (cell voltage: $V_{cell} = \Delta H_R/2F$ = 1.3 V). Increasing $\dot{Q}_{solar,th}$ increased the stack temperature, and enhanced the performance of the SOE stack, resulting in higher current densities at thermoneutral operation. The current density increased from j_{tn} = 435 A m^{-2} for $\dot{Q}_{solar,th}$ = 1.64 kW (T_{stack} = 856 K) to j_{tn} = 1265 A m^{-2} for $\dot{Q}_{solar,th}$ = 2.05 kW (T_{stack} = 967 K) for SFC 4/4, showing almost a tripling in current density at thermoneutral voltage when increasing $\dot{Q}_{solar,th}$ by 25% (i.e. the temperature by 111 K). This emphasizes the electrochemical advantage from high-temperature electrolysis (i.e. reduced kinetic and ohmic losses) allowing for higher thermoneutral current densities with increasing temperature. The measured thermoneutral current density increased from j_{TN} = 811 A m^{-2} for SFC

8

2/2 to j_{TN} = 1265 A m^{-2} for SFC 4/4, both for $\dot{Q}_{solar,th}$ = 2.05 kW, showing an increase of 56% when doubling the SFC. The current SOE stack showed limited current densities (<1500 A m^{-2}) at thermoneutral operation for stack temperatures T_{stack} < 1000 K. It was not possible to achieve higher stack temperatures (we aimed at 1050 K) and demonstrate the full performance of the SOE stack *in-situ* due to thermal limitations in the solar cavity-receiver (T_{cav} < 1150 K) and transmission losses. Extrapolations to higher temperatures predicted a thermoneutral current density of 5200 A m^{-2} for T_{stack} = 1050 K, which is comparable to state-of-the-art electrolyzers with current densities of ~8000 A m^{-2}.[28]

Integrated operation of solar reactor – The integrated solar reactor was tested for SFC 2/2 and SFC 4/4, for $\dot{Q}_{solar,th}$ ranging from 1.6 to 2.1 kW, and current densities ranging from 284 – 1265 A m^{-2}, thus the solar electrical input was $\dot{Q}_{solar,PV}$ = 0.1 – 0.4 kW. The total solar energy input (i.e. $\dot{Q}_{solar,th} + \dot{Q}_{solar,PV}$) ranged from 1.7 – 2.5 kW. The comparison of the cavity temperatures for SFC 4/4 obtained for campaign 2 to the ones measured in type 2 of campaign 1 were within 10% (largest error is uncertainty of solar thermal input), and thus reproducible. The STT efficiency for SFC 4/4 were also within 10% for campaign 2 and type 2 results of campaign 1. The STT efficiencies for SFC 2/2 (campaign 2, not measured in campaign 1) were lower and ranged from 3.46 – 3.95%. We measured a temperature difference between the solar cavity-receiver and the SOE stack – termed as the transmission losses – ranging from 103 – 137 K. Compared to the predicted temperature drop of 300 K of the work in[26], we reported a reduction in transmission losses by >50%, highlighting the advantage of the integrated design of the solar reactor.

The highest STH efficiency was η_{STH} = 3.33% obtained for the highest SFC (SFC 4/4) and largest solar thermal and solar electric input, i.e. $\dot{Q}_{solar,th}$ = 2.1 kW and $\dot{Q}_{solar,PV}$ = 0.4 kW. The Sankey diagram in Figure 4 shows the conversion of the solar thermal and electrical power in the solar reactor to hydrogen, quantifying the energy losses for the highest STH efficiency case (η_{STH} = 3.33%). The heat losses ($\dot{Q}_{loss}$ = 1.8 kW) in the solar cavity-receiver have the largest contribution (74% from total solar input $\dot{Q}_{solar,th} + \dot{Q}_{solar,th}$ =2.5 kW), which is mainly attributed to the insufficient insulation of the solar cavity-receiver resulting in a low STT efficiency (η_{STT} = 6.8%). Analogously to the thermal analysis, the reradiation losses ($\dot{Q}_{rerad}$ = 0.1 kW) are low (<5% from the total solar input), and thus are negligible. The second largest contribution are the PV losses ($\dot{Q}_{PV,loss}$ = 0.31 kW), which have a contribution of 12.6% of the total solar input. Transmission losses and DC-DC losses are negligible. The heat for the evaporation (Q_{evap} = 0.01 kW) of the reactant (liquid water) that is transformed to hydrogen is used for reducing the reaction enthalpy, and thus the electricity demand. In the Sankey diagram, we observe that the heat of evaporation is the only flow from the thermal process into the electrical process. Thus, the produced hydrogen ($\Delta \dot{n}_{H_2} \cdot HHV_{H_2}$ = 0.08 kW) is higher in power (by 0.01 kW) than the used electricity demand (P_{stack} = 0.07 kW). Note that heat for evaporation of excess water (given by overstoichiometry) cannot be used and leaves the thermal

9

process together with the other gases (i.e. $\Delta H_{stack} = 0.12$ kW). The solar factor was $f_{solar} = 84\%$, much higher than observed in the simulated reference case ($f_{solar} = 15\%$). This difference is resulting from *i*) the inefficient insulation of the solar cavity-receiver requiring additional solar thermal input and *ii*) the low SOE stack temperature resulting in a moderate thermoneutral current density, and thus also limiting the solar electrical input. The other experimental cases showed lower STH efficiencies and similar characteristics as the highest STH efficiency case (see Figure S10). All parameters and results for the experimental campaigns are listed in Table S3.

3. Conclusions

We investigated high-temperature electrolysis for water splitting using concentrated solar radiation. The reactants for the SOE stack are heated by absorbing solar radiation in a solar cavity-receiver. The electricity for the SOE stack is delivered by PV cells. In the first part, we implemented a lumped parameter model coupling radiative heat transfer in the solar cavity-receiver with the governing conservation and transport equations in the SOE stack in order to identify the best configuration for optimizing the STH efficiency and H_2 production rate, with particular attention to thermoneutral and endo/exothermal operation of the SOE stack. We predicted a STH efficiency of up to 19.85% (or 16.87% on a system level using a solar dish concentrator with optical efficiency of 85%) for the reference case (assuming $\tilde{C} = 500$, $\eta_{PV} = 20\%$, $f_{loss} = 20\%$), operating the SOE stack in endothermal mode. Using heat recovery with effectiveness of more than 10% (corresponding to a heat exchanger efficiency of >28.8%) enabled an increase in the STH efficiency, pushing it above 20%, and thus $\eta_{STH} > \eta_{PV}$. This means that the reduced solar electrical input for the SOE stack fully compensates the solar thermal input required for reactant heating and internal electrical DC-DC conversion losses, and thus the high-temperature electrolysis becomes beneficial.

This analysis was followed by a proof-of-concept of an integrated solar high-temperature electrolysis reactor. The integrated design comprised a double helical tube serving as a solar cavity-receiver, which absorbed concentrated solar radiation and heated the reactants for the SOE stack. The SOE stack was placed in the back of the solar cavity-receiver, in immediate proximity. The reactor was demonstrated for a solar power input of up to 2.5 kW (17% electrical and 83% thermal). For demonstration purposes, the SOE stack was powered by grid electricity with an assumed STE efficiency of 20% (PV cells) and no heat recovery was implemented ($\eta_{HR} = \eta_{HX} = 0$). The reactor was tested in EPFL's high-flux solar simulator (i.e. concentrations in the range of 717 to 1672). The SOE stack was characterized *in-situ* and revealed a maximum current density of 1265 A m^{-2} at thermoneutral operation for a stack temperature of 967 K (for the highest SFC 4/4 and highest solar thermal input of 2.1 kW). Endothermal operation was not possible due to safety concerns with the cavity. The corresponding highest STH efficiency measured was $\eta_{STH} = 3.33\%$ (resulting from SFC 4/4, $\dot{Q}_{solar,th} = 2.1$ kW, and $\dot{Q}_{solar,PV} = 0.4$ kW).

We demonstrate here for the first time an integrated solar high-temperature electrolysis concept, with reasonable efficiency and engineering solutions for improved performance. The integrated design reduced the transmission losses by more than 50% and the demonstration highlights the

10

benefit of the integrated design (SOE stack in immediate proximity of solar cavity-receiver). The large solar factor (of 84%) indicates the non-optimal solar cavity-receiver design resulting in a low STT efficiency of 6.8%, and consequently also in a low STH efficiency of 3.3%. The analysis indicated that a thermally efficient solar cavity-receiver is essential for reasonable operation temperatures in the SOE stack (~1050 K) yielding current densities of 3000 – 4000 A m^{-2}. We identify two main losses in the cavity-receiver, which were conduction heat loss from the double helix to the water-cooled aperture (front shield) and radiation heat loss from the double helix through the non-optimum insulation towards the reactor shell. Consequent decoupling of hot parts from cold parts and efficient insulation are expected to decrease the heat losses in the solar cavity-receiver. Furthermore, we claim that a scale-up of the current solar cavity-receiver design allows for higher thermal efficiencies as constructive constraints become less stringent (e.g. better accessibility of void spaces that can be better insulated or methods for decoupling hot from cold parts without scarifying the cavity effect, i.e. apparent absorptivity approaching 1). Furthermore, scaling of the reactor with improved surface to volume ratios will further decrease the relative importance of these heat losses. Additionally, the scale-up strategy is also expected to further reduce the transmission losses given the possibility of having higher reactant flow rates while the distance between the solar-cavity receiver and the SOE stack is kept constantly small. The use of heat recovery revealed less room for improvement and has to be considered as secondary approach for further improvements in the η_{STT} due to the limited enthalpy in the outlet gas streams (enthalpy stream, and thus the recoverable heat is only 35% compared to thermal solar input).

We expect from the computational analysis that a solar factor of around 15% (resulting from an STT efficiency larger than 60%) is necessary in order to make the high-temperature electrolysis interesting (i.e. energetically not yet beneficial but compared to room temperature electrolysis compatible, for example, given by abundant catalyst materials for SOE stacks compared to rare catalyst materials for room temperature electrolysis). The high-temperature electrolysis becomes energetically beneficial, resulting in STH efficiencies higher than the STE efficiency of the PV cells (and thus compensating reactant heating and internal electrical losses), for solar factors lower than 12%. Our analysis clearly shows the necessity of running the SOE stack in the endothermic mode enabling the beneficial high-temperature electrolysis. Finally, we found guidelines for best operation of solar-integrated high-temperature electrolysis of water and expect a similar behavior for the electrolysis of CO_2 (however no liquid-vapor phase transition, i.e. no gain from heat of evaporation), and thus allowing for improved solar-driven co-electrolysis.

4. Experimental procedures and modeling

Resource availability
Lead contact–Further information and requests for resources and materials should be directed to and will be fulfilled by the lead contact, Sophia Haussener (sophia.haussener@epfl.ch).
Materials availability–This study did not generate new unique materials.
Data and code availability–The source code used for the calculations and the data generated in this study are available from the corresponding author on reasonable request.

4.1. High-temperature electrolysis

The theoretical ETH efficiency of an electrolyzer is described by the ratio of the reaction enthalpy and Gibbs energy.[10] For electrolysis of water at standard conditions (300 K, 1 atm), $\eta_{theor}^0 = \Delta h_R^0 / \Delta g_R^0 = 1.05$ (with $\Delta g_R = \Delta h_R - T \cdot \Delta s_R$). The aim of high-temperature electrolysis is to increase the reaction temperature and thus *i*) reduce the reaction enthalpy by water's heat of evaporation, and *ii*) decrease the Gibbs energy in the gaseous state of water (i.e. to push the chemical equilibrium towards the products of H_2 and O_2). This results in a decrease of the standard equilibrium potential, $E_0 = \Delta g_R / (2F)$ (*F*=96'485 C mol^{-1}). The difference between the reaction enthalpy and the Gibbs energy is the maximum energy (the thermodynamic limit) that can be provided by heat instead of electricity. This amount is increased for high-temperature electrolysis compared to electrolysis at room temperature. The thermodynamic limit can only be approached when the electrolyzer is operated at the equilibrium potential, i.e. an unpractical operation with zero current density and H_2 production. More practical operation is at the thermoneutral voltage, given by $E_{tn} = \Delta H_R / (2F)$. However, the thermoneutral operation does not benefit from an increase in reaction temperature as the reaction enthalpy is nearly constant with temperature (except for heat of evaporation at the liquid-vapor phase transition). Thus, the electricity demand is constant with increasing temperature.

Generally, three different modes of electrolyzer operation can be considered. An endothermal mode in which the cell voltage is smaller than E_{tn}. External heat has to be provided (in order to maintain the cell temperature) and, thus, the electricity demand is reduced, resulting in an ETH efficiency higher than 1. A thermoneutral mode in which the cell voltage is equal to E_{tn}, and thus all energy for the reaction enthalpy is provided by electricity, resulting in an ETH efficiency equal to 1. And an exothermal mode in which the cell voltage is larger than E_{tn}, and thus the excess electricity produces internal heat, resulting in an ETH efficiency lower than 1. The reactant heating (sensible heat and evaporation of water) has to be taken into account separately for all considerations of high-temperature electrolysis. In general, heat recovery from the outlet gas stream is necessary for reasonable overall efficiencies.

4.2. Lumped parameter model of the integrated solar reactor

The modeled system includes a solar cavity-receiver for reactant heating and an Ni/YSZ/LSM SOE stack for the electrolysis of water. We developed a 0-dimensional lumped parameter model considering the corresponding governing conservation and transport equations for each component. The concentrated PV cells and heat exchangers for heat recovery were not explicitly modeled but assumed to operate with constant efficiencies. Other auxiliary components, such as pumps or compressors for the reactants and cooling water, were not modeled.

Solar cavity-receiver – An idealized blackbody solar cavity-receiver was assumed where the apparent absorptivity, $\alpha_{apparent}$, approaches 1. The energy conservation at steady-state is given:

$$\dot{Q}_{\text{thermal}} = \left[\overbrace{\sum_i \dot{n}_{i,\text{react}} \cdot \left(h_{i,\text{react}}\left(T_{\text{cav}}\right) - h_{i,\text{react}}\left(T_{\text{amb}}\right) \right)}^{\dot{Q}_{\text{absorbed}}} + \overbrace{A_{\text{aper}} \cdot \sigma \cdot \alpha_{\text{apparent}} \cdot \left(T_{\text{cav}}^4 - T_{\text{amb}}^4 \right)}^{\dot{Q}_{\text{reradiation}}} + \dot{Q}_{\text{loss}} \right], \quad (1)$$

where $\dot{Q}_{\text{thermal}}$ is the thermal input to the solar cavity-receiver (either directly the solar thermal input, $\dot{Q}_{\text{solar,th}}$, or $\dot{Q}_{\text{solar,th}}$ and the heat recovered from the products), $\dot{Q}_{\text{absorbed}}$ is the useful absorbed heat expressed as the enthalpy gain of all reactants, $\dot{n}_{i,\text{react}}$ is the molar flow rate of the reactant i, $h_{i,\text{react}}$ is the molar enthalpy of reactant i at ambient and cavity temperatures, T_{amb} and T_{cav}, $\dot{Q}_{\text{reradiation}}$ is the reradiation loss, A_{aper} is the aperture area of the solar cavity-receiver, σ the Stefan-Boltzmann constant, $\dot{Q}_{\text{loss}}$ are conductive and convective heat losses of the solar cavity-receiver (due to conduction through the insulated jacket and convection out of the aperture). We assessed the heat losses for varying conditions (see Supplementary Note 2) and concluded that they can be approximated with an constant loss factor, f_{loss} ($\dot{Q}_{\text{loss}} = f_{\text{loss}} \cdot \dot{Q}_{\text{thermal}}$). Heat recovery from the outlet steam enables the reduction of solar thermal input. The heat exchanger efficiency is defined $\eta_{\text{HEX}} = \dot{Q}_{\text{HEX}} / \Delta H_{\text{stack}}$, where $\dot{Q}_{\text{HEX}}$ is the extracted heat from the outlet stream's enthalpy, ΔH_{stack}. We assumed $\dot{Q}_{\text{thermal}} = \dot{Q}_{\text{solar,th}} \cdot \left(1 - \eta_{\text{HR}}\right)$ with η_{HR} the effectiveness of the heat recovery (see Supplementary Note 2 for discussion of heat recovery). η_{HEX} and η_{HR} represent the same phenomena but differently defined ($\eta_{\text{HR}} = 10\%$ is equivalent to $\eta_{\text{HX}} = 28.8\%$, $\eta_{\text{HR}} = 20\%$ is equivalent to $\eta_{\text{HX}} = 59.3\%$, and $\eta_{\text{HR}} = 30\%$ is equivalent to $\eta_{\text{HX}} = 83.8\%$). We neglected transmission losses from the solar cavity-receiver to the SOE stack, thus the stack temperature, T_{stack}, was only different from T_{cav} as a result of thermal effects of the electrochemical reactions (endo/exothermal SOE stack operation mode).

SOE electrolyzer – We followed the work in[29] for the implementation of a 0-dimensional, lumped parameter model considering the corresponding governing conservation and transport equations of the SOE stack. We assumed a Ni/YSZ/LSM SOE stack (Almus AG, UBOCELL solid oxide fuel cell mini stack, 100 W, later used for experimental demonstration). The cell voltage is given by:

$$V_{\text{cell}} = E + \eta_{\text{act,c}} + \eta_{\text{act,a}} + \eta_{\text{ohmic}} + \eta_{\text{conc,a}} + \eta_{\text{conc,a}}, \quad (2)$$

where E is the water splitting equilibrium voltage, $\eta_{\text{act,a}}$ and $\eta_{\text{act,c}}$ are the activation overpotentials at the anode and cathode, η_{ohmic} is the ohmic resistance (oxygen ion conduction through YSZ electrolyte), and $\eta_{\text{conc,a/c}}$ are the concentration overpotentials at the anode and cathode. The pressure in the gas channels is assumed to ambient pressure ($P_{\text{atm}} = 1$ atm). The equilibrium voltage is calculated by the Nernst equation $E = E_0 + \dfrac{R \cdot T_{\text{stack}}}{2 \cdot F} \ln\left[\dfrac{y_{H_2}^0 \cdot \left(y_{O_2}^0\right)^{1/2}}{y_{H_2O}^0} \right]$, where the standard equilibrium potential is approximated by $E_0 = 1.253 - 2.4516 \times 10^{-4} T_{\text{stack}}$, R is the universal gas

constant (8.3145 J mol^{-1} K^{-1}), and $y_{H_2O}^0$, $y_{H_2}^0$, and $y_{O_2}^0$ are the molar fractions of steam, hydrogen, and oxygen at the channel-electrode interface. The activation overpotentials are calculated by

$\eta_{act,i} = \dfrac{R \cdot T_{stack}}{F} \text{arcsinh}\left(\dfrac{J}{2 \cdot J_{0,i}}\right)$, where J is the electrical current density, $J_{0,i}$ is the exchange

current density for the anode ($i = a$) and cathode ($i = c$), which are expressed by

$J_{0,i} = \gamma_i \cdot \left(-\dfrac{E_{act,i}}{R \cdot T_{stack}}\right)$ with γ_i as pre-exponential factor and $E_{act,i}$ as the activation energy. The

ohmic overpotential is calculated according to $\eta_{ohmic} = 2.99 \times 10^{-5} \cdot J \cdot L \cdot \exp\left(\dfrac{10300}{T_{stack}}\right)$, where L is

the thickness of the electrolyte in microns. The concentration overpotentials are approximated

using Fick's model[30] resulting in $\eta_{conc,a} = \dfrac{R \cdot T_{stack}}{2 \cdot F} \ln\left[\left(1 + \dfrac{R \cdot T_{stack}}{D_{O_2}^{eff} \cdot P_{atm} \cdot y_{O_2}^0} \cdot \dfrac{J}{4 \cdot F} \cdot d_a\right)^{1/2}\right]$ and

$\eta_{conc,c} = \dfrac{R \cdot T_{stack}}{2 \cdot F} \ln\left[\dfrac{1 + J \cdot R \cdot T_{stack} \cdot d_c / \left(2 \cdot F \cdot D_{H_2O}^{eff} \cdot P_{atm} \cdot y_{H_2}^0\right)}{1 - J \cdot R \cdot T_{stack} \cdot d_c / \left(2 \cdot F \cdot D_{H_2O}^{eff} \cdot P_{atm} \cdot y_{H_2O}^0\right)}\right]$, where the effective diffusion

coefficients of oxygen and steam are approximated by $D_{O_2}^{eff} = 4.2677 \times 10^{-9} \cdot T_{stack}^{1.75}$ and

$D_{H_2O}^{eff} = 9.5597 \times 10^{-10} \cdot T_{stack}^{1.75}$ and d_a and d_c are the thicknesses of the anode and cathode.

The SOE stack was considered to be operated in all three modes (i.e. endothermal, thermoneutral, and exothermal). Given the enthalpy stream from the solar cavity-receiver, $H_{cav} = \sum_i \dot{n}_{i,react} \cdot h_{i,react}(T_{cav})$, the enthalpy stream leaving the SOE stack can be written:

$$H_{stack} = H_{cav} + I_{stack} \cdot N_{cell} \underbrace{\left[\overbrace{\left(V_{cell} - E\right)}^{\text{Joule heating}} - \overbrace{\dfrac{1}{2 \cdot F} \cdot \left(T_{stack} \cdot \Delta S_R\right)}^{\text{Reaction heat sink}}\right]}_{\dot{Q}_{stack}} = \sum_i \dot{n}_{i,prod} \cdot h_{i,prod}(T_{stack}), \qquad (3)$$

where I_{stack} is the electric current of the SOE stack and N_{cell} is the number of (in-series) cells in the SOE stack. Note that the Joule heating coming from all overpotentials adds heat whereas the reaction removes heat from the SOE stack. The sum of both terms is the thermal effect of the electrochemical reaction – termed heat flux of the SOE stack, $\dot{Q}_{stack}$. Thus, H_{stack} can be smaller, equal or larger than H_{cav} depending on the operation mode (i.e. endothermal, thermoneutral, and exothermal). The stack temperature is then retrieved from the enthalpy stream leaving the SOE stack. We considered a temperature range of $900 - 1300$ K and a current density range of $0 - 5000$ A m^{-2} of the stack (state-of-the-art electrolyzers operate up to current densities of ~8000 A m^{-2}).[28]

Table 1. Parameters used in 0D model (thermal and electrochemical)

Parameter	Symbol	Unit	Value	Reference
Solar concentration	$\tilde{C}$	-	250 - 750	[27]
Heat loss factor	f_{loss}	-	0.1 - 0.3	[27]
Heat recovery effectiveness	η_{HR}	-	0.0 - 0.3	[27]
Pre-exponential factor for anode exchange current density	γ_a	A m^{-2}	2.051 x 10^9	[29]
Pre-exponential factor for cathode exchange current density	γ_c	A m^{-2}	1.344 x 10^{10}	[29]
Activation energy for anode	$E_{act,a}$	J mol^{-1}	1.2 x 10^5	[29]
Activation energy for cathode	$E_{act,c}$	J mol^{-1}	1.0 x 10^5	[29]
Electrolyte thickness	L	μm	13	Almus AG
Cathode thickness	d_c	μm	250	Almus AG
Anode thickness	d_a	μm	50	Almus AG
Overstoichiometry factor	$f_{overstoich}$	-	2	assumed
Current density	J	A m^{-2}	500 - 5000	assumed
Stack area	A_{stack}	cm^2	432	Almus AG
Stack flow conditions	SFC	Nml min^{-1} cm^{-2}	0.6 - 7	assumed
Solar-to-electricity efficiency of PV cells	η_{PV}	-	0.2	assumed
DC-DC-converter efficiency	η_{DC-DC}	-	0.93	assumed

The current density and the specific solar thermal input (solar thermal input per area of the SOE stack) served as input parameters for the model. We followed the recommended stack flow conditions (SFCs) by Almus AG for the flow rates of the reactants (see section 4.4) using the same specific flow rate (i.e. Nml min^{-1} cm^{-2}) for H_2O in the cathode (with additionally 10%-molar H_2) and air in the anode. The flow rates are linked to the current density given the constant overstoichiometry. All parameters are listed in Table 1.

4.3. Performance metrics
The required solar power input for the PV cell is:

$$\dot{Q}_{solar,PV} = \frac{I_{stack} \cdot V_{stack}}{\eta_{PV} \cdot \eta_{DC-DC}} \tag{4}$$

where $V_{stack} = N_{cell} \cdot V_{cell}$ is the voltage of the SOE stack (cells in-series), $\eta_{PV} = 20\%$ and $\eta_{DC-DC} = 93\%$ are the assumed STE efficiency of the PV cells (single-junction crystalline silicon PV cell) and the DC-DC converter efficiency, respectively.[9]

The STT efficiency of the solar cavity-receiver is defined as:

$$\eta_{STT} = \frac{\dot{Q}_{absorbed}}{\dot{Q}_{thermal}} , \tag{5}$$

and is independent of the heat recovery effectiveness. The solar power input fraction is defined:

$$f_{solar} = \dot{Q}_{solar,th} / \left(\dot{Q}_{solar,th} + \dot{Q}_{solar,PV} \right). \tag{6}$$

The limit of the STT efficiency is given by the ideal solar cavity-receiver efficiency (accounting for heat losses):

$$\eta_{STT,limit} = 1 - f_{loss} - \sigma \cdot \alpha_{apparent} \frac{T_{cav}^4 - T_{amb}^4}{\tilde{C} \cdot E_{bn}}. \tag{7}$$

The STH efficiency is defined:

$$\eta_{STH} = \frac{\Delta \dot{n}_{H_2} \cdot HHV_{H_2}}{\dot{Q}_{solar,PV} + \dot{Q}_{solar,th}}, \tag{8}$$

where $\Delta \dot{n}_{H_2}$ denotes the molar rate of produced hydrogen and HHV_{H_2} is the higher heating value of hydrogen for standard conditions (286 kJ mol^{-1}). The Faradaic efficiency of the SOE stack was assumed to 100%.[31] Hence, the produced hydrogen was calculated by $\Delta \dot{n}_{H_2} = N_{cell} \cdot I_{stack} / (2 \cdot F)$.

The overstoichiometry is defined as $f_{overstoich} = \dfrac{\dot{n}_{H_2O}}{\Delta \dot{n}_{H_2O}}$, where $\dot{n}_{H_2O}$ is the actual molar flow rate of water and $\Delta \dot{n}_{H_2O}$ is the molar flow rate of consumed water (and due to conservation of species $\Delta \dot{n}_{H_2O} = \Delta \dot{n}_{H_2}$). Note, the STH efficiency (on the reactor level) is directly correlated to the STH efficiency on the system level (which accounts for the optical losses in the solar concentrator) as both solar thermal and solar electrical inputs are concentrated solar radiation, and thus originating from the same solar concentrator. Consequently, $\eta_{STH.system} = \eta_{STH} \cdot \eta_{concentrator}$, where $\eta_{concentrator}$ is the optical efficiency of the concentrator. Reported optical efficiencies are $\eta_{concentrator} = 78 - 89\%$ for solar dishes and $\eta_{concentrator}$ up to 70% for solar towers.[32,33] To keep our analysis general, we did not include a detailed optical analysis that would strongly depend on plant scale, location, reactor configuration etc.

We assumed for the estimation of the limit of the STH efficiency i) the thermodynamic limit of electrochemical conversion ($\Delta h_R / \Delta g_R$), ii) solar cavity-receiver accounting for additional heat losses, iii) heat recovery, iv) only water with $f_{overstoich} = 1$, no other reactants, and thus only enthalpy heating of water (no excess water, all water is converted into H$_2$), and v) Faradaic efficiency of 100%:

$$\eta_{STH,limit} = \frac{HHV_{H_2}}{\underbrace{\frac{1}{\eta_{STT,limit}} \cdot \left[(1-\eta_{HR}) \cdot \left(h_{H2O}(T_{cav}) - h_{H2O}(T_{amb}) + T_{stack} \cdot \Delta S \right) \right]}_{thermal} + \underbrace{\frac{1}{\eta_{PV} \cdot \eta_{DC\text{-}DC}} \cdot \left(\Delta h_R - T_{stack} \cdot \Delta s_R \right)}_{electrochemical}} \tag{9}$$

4.4. Experimental setup

We followed the design guidelines of the work in[34] for the design of the solar cavity-receiver where a numerical model has been implemented consisting of a detailed 1D two-phase flow model in the absorber tubes coupled to a 3D heat transfer model in the solar cavity-receiver providing guidance on operation and design of such direct steam generators. The best configuration from several designs incorporated a helically-shaped absorber tube predicting a STT efficiency of 80%. Thus, we implemented two helically shaped interlaced absorber tubes enabling the heating of the two reactants (water/hydrogen and sweep gas). For demonstration purposes, we *i*) used a commercial SOE stack, *ii*) did not implement PV cells for electricity production but used external electricity from the grid and assumed $\eta_{STE} = 20\%$ accordingly, and *iii*) did not implement heat recovery.

A scheme of the 2.5 kW integrated solar reactor coupling a double helical tube solar cavity-receiver and a 16-cell SOE stack as well as auxiliary components is shown in Figure 5 and photos of the setup in Supplementary Note 8. The stainless steel (304 L) shell's length is 300 mm and its diameter is 305 mm. The shell was mounted between two steel flanges with 395 mm diameter and 20 mm thickness. The water-cooled front consists of a double flange. One flange comprised a spiral 8 mm^2 cooling-water duct. The shell and three flanges were fixed by 12×M20 screws and mounted on a base plate serving as stand.

Solar cavity-receiver – The solar cavity-receiver (red dotted line in Figure 5) comprised the double helical tube (tube inner diameter 5 mm, outer diameter 6 mm, helical turning radius 40 mm, and pitch of each helix 12.2 mm, made of Inconel 600) mounted to the reactor's circular aperture (cone top diameter of 40 mm, cone bottom diameter 72 mm, cone angle 45°) to separate reactant heating of the anodic (air or N_2) and cathodic gases (H_2 and H_2O). The water-cooled aperture was windowless allowing for the direct incidence of concentrated solar radiation onto the absorber surface. The cone angle of the aperture was chosen according to the 45° rim angle of EPFL's HFSS.[35] The apparent absorptivity exceeded the inner surface absorptivity α due to the cavity-like geometry of the double helix allowing for multiple reflections. Here, $\alpha_{apparent}$ exceeds 0.98 for an assumed absorptivity of the inner surfaces of $\alpha > 0.6$, and thus the solar cavity-receiver approached a blackbody absorber.[36]

SOE stack – A commercial SOE stack (Almus AG, UBOCELL solid oxide fuel cell mini stack, 100 W) was mounted at the rear of the solar reactor (green dotted line in Figure 5) and operated in the electrolysis mode. The SOE stack was composed of 16 square cathode-supported cells, each cell with a size of 36 cm^2 and an active surface of 27 cm^2. Thus, the total active area of the stack was 432 cm^2. Cells were stacked and electrically connected in series by steel bipolar plates. The cathode of the SOE cell was made of Ni-cermet with a thickness of 250 μm. The YSZ membrane with a thickness of 13 μm acted as solid electrolyte for oxygen ion transport. The anode was made of LSM with a thickness of 50 μm. We assumed a Faradaic efficiency of 100% given that the stack was not run at extreme overpotentials. Only such large potentials (>1.8 V per cell) could cause parasitic reactions, and consequently decrease the Faradaic efficiency.[37]

Reactant / sweep gas – Air or N_2 (sweep gas), representing the anode flow, and liquid water (reactant) premixed with H_2, representing the cathode flow, were separately piped at ambient

temperature and ambient pressure to the two inlets of the double helical tube (anode and cathode inlets in Figure 5). The 10%-molar H_2 in the cathode flow is added to prevent the Ni catalyst at the cathodes from re-oxidation. The reactants were then heated in the solar cavity-receiver. The specific flow rates are listed in Table S3.

Insulation – The space between the double helical tube, the SOE stack and the surrounding steel shell was thermally insulated by alumina fiber paper (Kaowool 1600, thermal conductivity: 0.0178 $W m^{-1} K^{-1}$ at ambient temperature).

High-flux solar simulator – The EPFL's 45 kW_e HFSS consists of 18 ellipsoidal Xe arc lamps with common focus mimicking real sun concentrators, such as solar dishes or solar towers. The total radiative power is > 7.5 kW and the peak concentration exceeds > 20 $kW m^{-2}$. The radiative power distribution was measured by a calibrated charge-coupled device (CCD) camera.[38] The accuracy of the radiative power distribution is estimated to 10%.[39] The solar reactor was positioned at the focal plane of the HFSS. The solar thermal input entering the reactor (solar cavity-receiver) was computed by integrating the measured radiative flux over the reactor's aperture.

Flow diagram of the experimental setup – The deionized liquid water was provided by a dosing pump (KNF SIMDOS 02, range 30 $\mu L min^{-1}$ – 20 ml min^{-1}, repeatability 1%). H_2 was generated by a H_2-generator (Swissgas, HG 6.0, range 0 – 1000 Nml min^{-1}, purity 99.9999%) and fed by a flow controller (Bronkhorst F-201CV, range 0 – 2 Nl min^{-1}, accuracy < 3%). Both inlet flows were mixed before injecting to the cathode tube. We expected fluctuations coming from the two-phase flow to be negligible due to fast phase transition, which was confirmed by time-resolved measurements of the production rates. The air (or alternatively N_2) was provided from a gas cylinder (Carbagas, synthetic air: 80% N_2, 20% O_2, accuracy <10%; nitrogen: 99.999% purity) and fed by a flow controller (Bronkhorst F-202AV, range 0 – 114 Nl min^{-1}, accuracy < 3%). The inlet flows were at room temperature and ambient pressure. The outlet anodic flow was directly released to the vent whereas the outlet cathodic flow (H_2 and steam) was cooled to ambient temperature by a condenser (Alfa Laval AN27-10H, counterflow, 5.5 kW_{th}). The H_2 was then separated from the remaining liquid water by a separator and released to the vent. Several K-type thermocouples (precision ±2 K) were used to monitor T_{cav} and the fluid temperatures, $T_{cathode}$ and T_{anode}, between the solar cavity-receiver and the SOE stack in the anode and cathode tube, respectively, and T_{stack} (placed in the center, fixed in a bipolar plate). Current-voltage characteristics of the SOE stack were measured in a 4-wire configuration using a power supply (Power Supply EA - PS 8080-60 DT, 0 – 80 V, 0 – 1500 W_{el}, accuracy <2%) driving the current and an electronic load used in voltmeter mode (DC Electronic Load EA-EL 3160-60, 0 – 160 V, 0 – 400 W_{el}, accuracy <2%) for the voltage measurement. The heating and cooling rate for the SOE stack was limited to a maximum of 200 K h^{-1} to avoid mechanical failure induced by thermal stress in the SOE stack. Thus, the heat up and cool down process of the integrated reactor setup was fully controlled by an electric heating tape (Ultra-High Temperature Heating Tape, Omega, STH102-060*, size 1" x 6', 940 W_{th}, not shown in Figure 5), which enclosed the SOE stack entirely.

Experimental campaigns – Two experimental campaigns were carried out in EPFL's HFSS. The thermal performance of the solar cavity-receiver was characterized in campaign 1 including two

types of tests. Type 1 tests consisted of runs without the SOE stack and aimed at thermal characterization. The operational conditions included N_2 in the anode and H_2O in the cathode side with flow rates ranging from 0.18 – 1.0 Nl min^{-1} and 2.25 – 12.6 g s^{-1}, respectively, and a solar thermal power input ($\dot{Q}_{solar,th}$) of 0.91 kW using three lamps of the HFSS with an average solar concentration of 724 (i.e. flux of 724 kW m^{-2}). These conditions were chosen to probe the optimized STT efficiencies of the proposed solar cavity-receiver. However, these flow conditions turned out to be less relevant, practical and safe for the subsequent operation with the SOE stack. Consequently, type 2 tests were designed, aiming at more relevant conditions for the integrated reactor (including SOE stack), and consisted of runs with the SOE in open circuit condition and for stack flow conditions (SFCs) with 4/4 (4 Nml min^{-1} cm^{-2} air at anode and 4 Nml min^{-1} cm^{-2} H_2O at cathode) and SFC 8/8 (8 Nml min^{-1} cm^{-2} air at anode and 8 Nml min^{-1} cm^{-2} H_2O at cathode), and a solar thermal input ($\dot{Q}_{solar,th}$) ranging from 0.9 – 2.1 kW using up to six lamps of the HFSS and with an average solar concentration of 717 to 1672. The *in-situ* characterization of the SOE stack and the testing of the performance of the integrated reactor were achieved in campaign 2. The setup was investigated for SFC 2/2 (2 Nml min^{-1} cm^{-2} air at anode and 2 Nml min^{-1} cm^{-2} H_2O at cathode) and SFC 4/4, and a solar thermal input ($\dot{Q}_{solar,th}$) of 1.6-2.1 kW using up to six lamps of the HFSS with average concentrations of 1274 to 1672, and solar power input to the PV cells of 0.1 – 0.4 kW (based on assumed STE efficiency of 20%). Considering the total active area of the stack (432 cm^2) and taking into account 10% H_2 (molar fraction with respect to H_2O) in the cathode tube, the detailed volumetric and mass flow rates are listed in Table S3.

Author Contributions
Conceptualization, M.L., C.S., and S.H.; Writing – Original Draft, M.L., C.S., and S.H.; Investigation, M.L. and C.S.; Software, M.L. and C.S.; Funding Acquisition, S.H.; Writing – Editing and Review, S.D., and J.V.H.

Declaration of Interests
The authors declare no competing interests.

References
1.   Kondratenko, E. V., Mul, G., Baltrusaitis, J., Larrazábal, G.O., and Pérez-Ramírez, J. (2013). Status and perspectives of CO2 conversion into fuels and chemicals by catalytic, photocatalytic and electrocatalytic processes. Energy Environ. Sci. *6*, 3112–3135.
2.   Ebbesen, S.D., Jensen, S.H., Hauch, A., and Mogensen, M.B. (2014). High temperature electrolysis

in alkaline cells, solid proton conducting cells, and solid oxide cells. Chem. Rev. *114*, 10697–10734.

3.   Foit, S.R., Dittrich, L., Vibhu, V., Vinke, I.C., Eichel, R.-A., and de Haart, L.G. (2017). Co-Electrolysis , Quo Vadis. In ECS Transactions, pp. 3139–3147.

4.   Scamman, D., Bustamante, H., Hallett, S., and Newborough, M. (2014). Off-grid solar-hydrogen generation by passive electrolysis. Int. J. Hydrogen Energy *39*, 19855–19868.

5.   AlZahrani, A.A., Dincer, I., and Naterer, G.F. (2013). Performance evaluation of a geothermal based integrated system for power, hydrogen and heat generation. Int. J. Hydrogen Energy *38*, 14505–14511.

6.   Ratlamwala, T.A.H., and Dincer, I. (2015). Comparative energy and exergy analyses of two solar-based integrated hydrogen production systems. Int. J. Hydrogen Energy *40*, 7568–7578.

7.   Ratlamwala, T.A.H., Dincer, I., and Aydin, M. (2012). Energy and exergy analyses and optimization study of an integrated solar heliostat field system for hydrogen production. Int. J. Hydrogen Energy *37*, 18704–18712.

8.   Zamfirescu, C., and Dincer, I. (2014). Assessment of a new integrated solar energy system for hydrogen production. Sol. Energy *107*, 700–713.

9.   Haussener, S., Hu, S., Xiang, C., Weber, A.Z., and Lewis, N.S. (2013). Simulations of the irradiation and temperature dependence of the efficiency of tandem photoelectrochemical water-splitting systems. Energy Environ. Sci. *6*, 3605–3618.

10. O'Brien, J.E. (2008). Thermodynamic Considerations for Thermal Water Splitting Processes and High Temperature Electrolysis. In ASME International Mechanical Engineering Congress and Exposition, pp. 1–13.

11. Laguna-Bercero, M.A.A. (2012). Recent advances in high temperature electrolysis using solid oxide fuel cells: A review. J. Power Sources *203*, 4–16.

12. Arashi, H., Naito, H., and Miura, H. (1991). Hydrogen production from high-temperature steam electrolysis using solar energy. Int. J. Hydrogen Energy *16*, 603–608.

13. Aguiar, P., Adjiman, C.S., and Brandon, N.P. (2004). Anode-supported intermediate temperature direct internal reforming solid oxide fuel cell. I : model-based steady-state performance. J. Power Sources *138*, 120–136.

14. AlZahrani, A.A., and Dincer, I. (2016). Design and analysis of a solar tower based integrated system using high temperature electrolyzer for hydrogen production. Int. J. Hydrogen Energy *41*, 8042–8056.

15. Balta, M.T., Kizilkan, O., and Yilmaz, F. (2016). Energy and exergy analyses of integrated hydrogen production system using high temperature steam electrolysis. Int. J. Hydrogen Energy *41*, 8032–8041.

16. Houaijia, A., Roeb, M., Monnerie, N., and Sattler, C. (2015). Solar power tower as heat and electricity source for a solid oxide electrolyzer: a case study. Int. J. Energy Res. *39*, 1120–1130.

17. Sanz-Bermejo, J., Muñoz-Antón, J., Gonzalez-Aguilar, J., and Romero, M. (2014). Optimal integration of a solid-oxide electrolyser cell into a direct steam generation solar tower plant for zero-emission hydrogen production. Appl. Energy *131*, 238–247.

18. Lin, M., and Haussener, S. (2017). Techno-economic modeling and optimization of solar-driven high-temperature electrolysis systems. Sol. Energy *155*, 1389–1402.

19. Koumi Ngoh, S., Ayina Ohandja, L.M., Kemajou, A., and Monkam, L. (2014). Design and simulation of hybrid solar high-temperature hydrogen production system using both solar photovoltaic and thermal energy. Sustain. Energy Technol. Assessments *7*, 279–293.

20. Steinfeld, A., and Schubnell, M. (1993). Optimum aperture size and operating temperature of a solar cavity-receiver. Sol. Energy *50*, 19–25.

21. Reddy, K.S., Vikram, T.S., and Veershetty, G. (2015). Combined heat loss analysis of solar parabolic dish – modified cavity receiver for superheated steam generation. Sol. Energy *121*, 78–93.

22. Zapata, J.I., Asselineau, C., Pye, J., Kaufer, M., and Hughes, G. (2014). An Integrated Optical and Thermal Model of Cavity Receivers for Paraboloidal Dish Concentrators. In Solar Research Conference, pp. 1–9.

23. Wang, P., Liu, D.Y., and Xu, C. (2013). Numerical study of heat transfer enhancement in the receiver tube of direct steam generation with parabolic trough by inserting metal foams. Appl. Energy *102*, 449–460.
24. Tembhurne, S., and Haussener, S. (2019). Controlling strategies to maximize reliability of integrated photo-electrochemical devices exposed to realistic disturbances. Sustain. Energy Fuels *3*, 1297–1306.
25. Schiller, G., Lang, M., Szabo, P., Monnerie, N., von Storch, H., Reinhold, J., and Sundarraj, P. (2019). Solar heat integrated solid oxide steam electrolysis for highly efficient hydrogen production. J. Power Sources *416*, 72–78.
26. Lin, M., and Haussener, S. (2018). An integrated concentrated solar fuel generator utilizing a tubular solid oxide electrolysis cell as solar absorber. J. Power Sources *400*, 592–604.
27. Lin, M., and Haussener, S. (2015). Solar fuel processing efficiency for ceria redox cycling using alternative oxygen partial pressure reduction methods. Energy *88*, 667–679.
28. Wang, L., Pérez-Fortes, M., Madi, H., Diethelm, S., van Herle, J., and Maréchal, F. (2018). Optimal design of solid-oxide electrolyzer based power-to-methane systems: A comprehensive comparison between steam electrolysis and co-electrolysis. Appl. Energy *211*, 1060–1079.
29. Ni, M., Leung, M.K.H., and Leung, D.Y.C. (2007). Parametric study of solid oxide steam electrolyzer for hydrogen production. Int. J. Hydrogen Energy *32*, 2305–2313.
30. Krishna, R., and Wesselingh, J.A. (1997). The Maxwell-Stefan approach to mass transfer. Chem. Eng. Sci. *52*, 861–911.
31. Dönitz, W., and Erdle, E. (1985). High-temperature electrolysis of water vapor—status of development and perspectives for application. Int. J. Hydrogen Energy *10*, 291–295.
32. Stine, W.B., and Diver, R.B. (1994). A compendium of solar dish/Stirling technology.
33. Corsi, C., Blanco, M.J., Grigoriev, V., and Pye, J. (2022). Upper limits to the mean annual optical efficiency of solar mono-tower systems. Sol. Energy *236*, 88–99.
34. Lin, M., Reinhold, J., Monnerie, N., and Haussener, S. (2018). Modeling and design guidelines for direct steam generation solar receivers. Appl. Energy *216*, 761–776.
35. Bader, R., Haussener, S., and Lipinski, W. (2014). Optical Design of Multisource High-Flux Solar Simulators. J. Sol. Energy Eng. *137*, 021012–1/9.
36. Steinfeld, A. (1991). Apparent absorptance for diffusely and specularly reflecting spherical cavities. Int. J. Heat Mass Transf. *34*, 1895–1897.
37. Schefold, J., Brisse, A., and Zahid, M. (2009). Electronic Conduction of Yttria-Stabilized Zirconia Electrolyte in Solid Oxide Cells Operated in High Temperature Water Electrolysis. J. Electrochem. Soc. *156*, B897–B904.
38. Levêque, G., Bader, R., Lipiński, W., and Haussener, S. (2016). Experimental and numerical characterization of a new 45 kWel multisource high-flux solar simulator. Opt. Express *24*, 1360–1373.
39. Guillot, E., Alxneit, I., Ballestrin, J., Sans, J.L., and Willsh, C. (2014). Comparison of 3 Heat Flux Gauges and a Water Calorimeter for Concentrated Solar Irradiance Measurement. Energy Procedia *49*, 2090–2099.
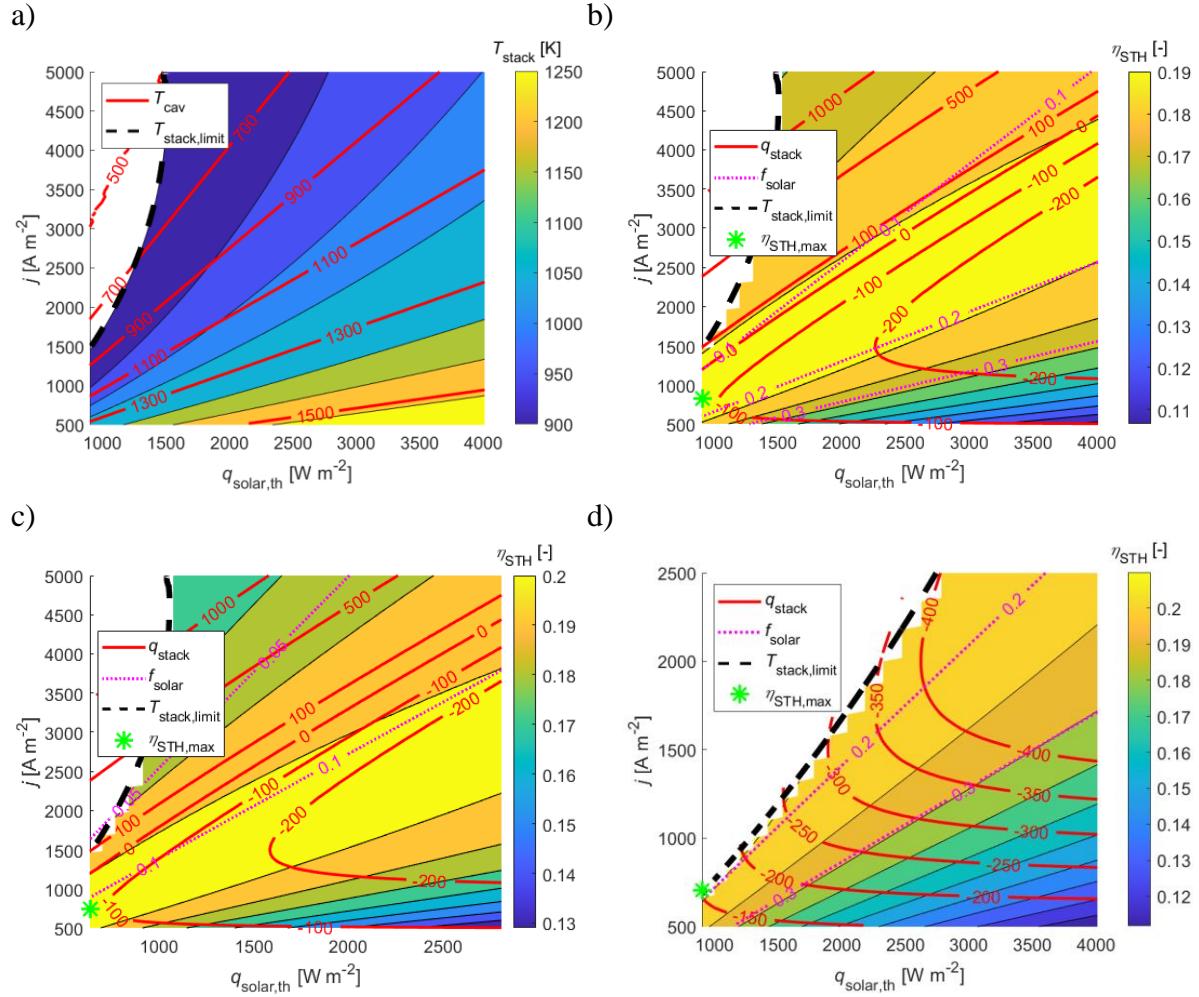
Figure 1. a) Temperatures of solar cavity-receiver (red solid isolines) and stack (contour plot) and b)-d) STH efficiency (contour plot), heat flux of SOE stack (red solid isolines), and solar power input fraction (magenta dotted isolines) as a function of solar thermal input and current density. Concentration was constant at $\tilde{C} = 500$, black dashed lines indicate lower (900 K) and upper (1300 K) stack temperature limit, solar thermal input range is 39 – 173 W, and solar PV input range is 132 – 1842 W. The reference case b) without heat recovery (19.85% maximum STH efficiency), c) with $\eta_{HR} = 30\% \;\hat{=}\; \eta_{HX} = 83.8\%$ (20.83% maximum STH efficiency), and d) with improved stack (21.16% maximum STH efficiency).
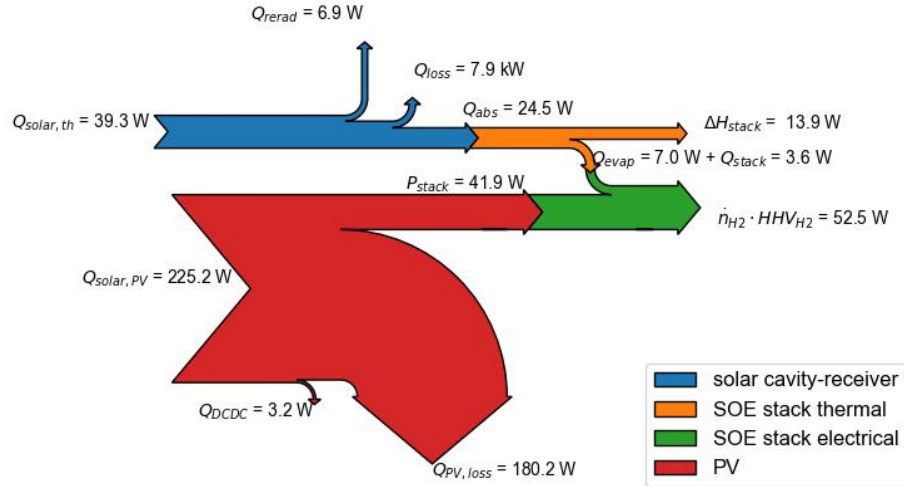
Figure 2. Sankey diagram of the solar integrated reactor indicating the energy repartition, starting with solar thermal and electrical input power and ending at the produced hydrogen output. The depicted case is for the simulated reference case with $\eta_{\text{STH,max}} = 19.85\%$, $q_{\text{solar,th}} = 910 \text{ W m}^{-2}$ and $q_{\text{solar,PV}} = 5213 \text{ W m}^{-2}$.
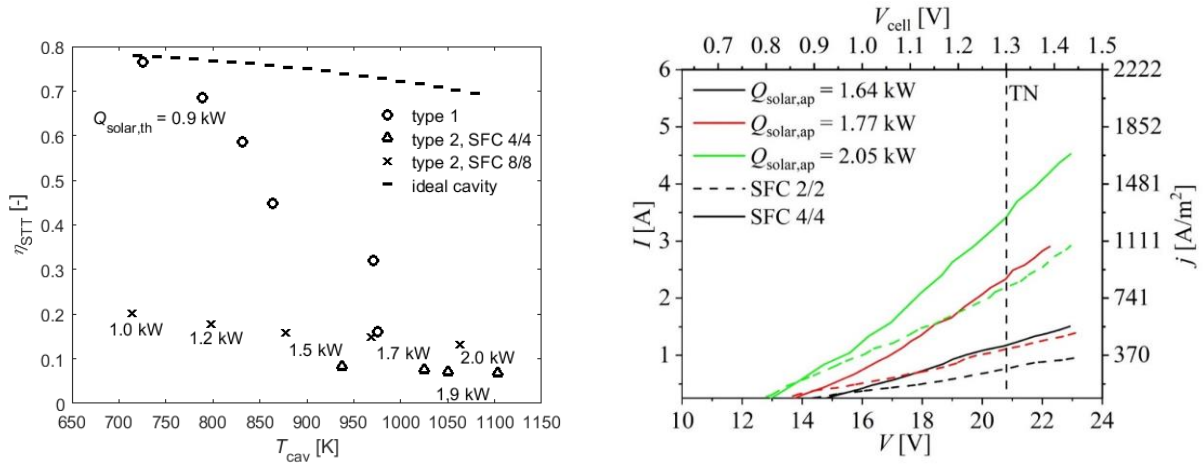
Figure 3. a) STT efficiency as a function of the cavity temperature. The circle and triangle/cross markers indicate type 1 and type 2 data of campaign 1, respectively. The dashed line represents an ideal solar cavity-receiver ($f_{\text{loss}} = 20\%$, $\tilde{C} = 724$). b) Measured current (density) versus voltage characteristics for the SOE stack operated at SFC 2/2 and SFC 4/4 for various stack temperatures. The thermoneutral stack voltage was $V_{\text{stack}} = 20.8 \text{ V}$ ($V_{\text{cell}} = 1.3 \text{ V}$ per cell).
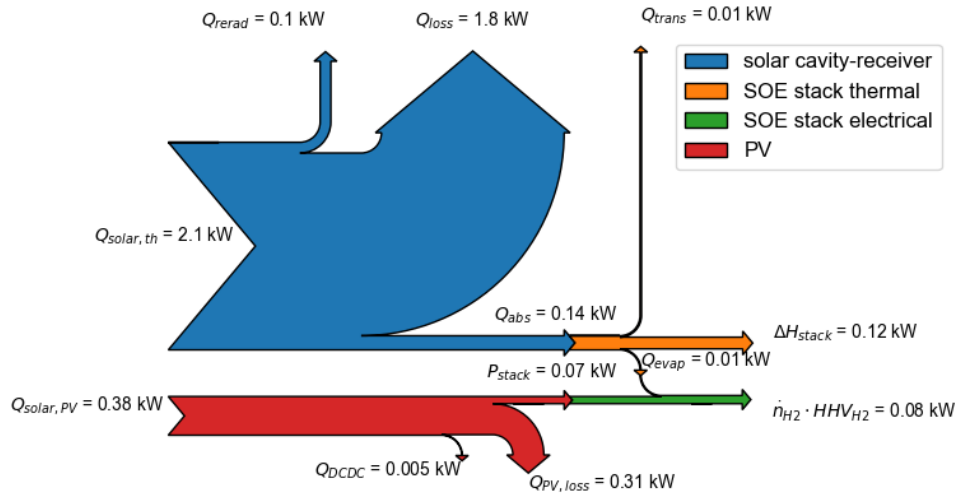
Figure 4. Sankey diagram showing the conversion of solar thermal and electrical input power to hydrogen for the solar cavity-receiver, PV cells and SOE stack. The depicted case is for the highest STH efficiency ($\eta_{STH} = 3.33\%$) for SFC 4/4 and $\dot{Q}_{solar,th} = 2.05$ kW and $\dot{Q}_{solar,PV} = 0.4$ kW.
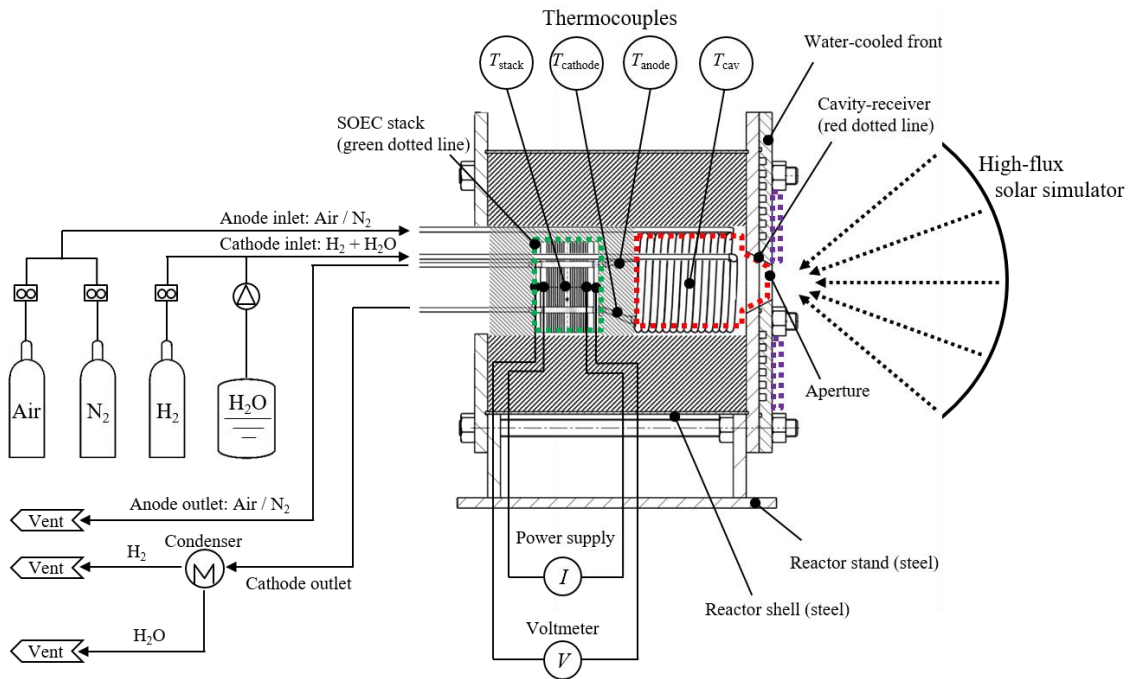
Figure 5. Schematic of the test setup, including the integrated solar reactor, EPFL's HFSS, and the fluidic and electrical connections and auxiliary devices. The reactor comprises a double helical tube (denoted by the red dotted line) and a 16-cell SOE stack (denoted by the green dotted line). Possible location of PV cells on the water-cooled front is indicated (violet dotted line). Indicated are the locations of the K-type thermocouples, power supply, voltmeter, inlet and outlet gas flows.